Chapter 3

Structural properties of pure metals and alloys

3.1 Introduction

The discovery of new generations of BMG's was guided by qualitative reasoning about relative melting and crystallization temperatures of various phases and the role of atomic size ratio (topological disorder) and valence electron configuration (chemical disorder) in promoting glass formation while frustrating crystallization (Johnson, 1998). In particular, the atomic size ratio is a crucial parameter in frustrating the crystallization (Egami and Waseda, 1984; Qi *et al.*, 1999). Although such qualitative ideas have been useful in making progress, it would be valuable to construct more rigorous theory relating the size ratio effect to glass formation to predict the glass forming behavior of more complex alloys. In addition to that, knowledge of the size ratio effect on the local ordering and phase separation behavior in the glass forming liquid would be interesting both scientifically and for industrial applications, such as controlling of crystallization, fabrication of composites, and production of multiphase *in situ* composites by partial crystallization.

As a first step toward providing this more quantitative understanding and the detailed knowledge of the local ordering and phase separation behavior, we report here systematic studies of the glass forming properties for a series of binary and ternary metallic alloys as a function of the atomic size ratio (l). These studies use Molecular Dynamics (MD) with the Sutton-Chen (SC) many-body force field developed to described metallic systems (Sutton and Chen, 1990).

We find three regimes of phase behavior upon cooling at a rate of 4×10^{12} K/s, defined by the magnitude of the size ration l ($l \leq 1.0$). When l is close to 1.0, the crystallization occurs upon cooling. In the alloy with $l \leq 0.95$, glass transition occurs. Examining the details of the changes of structure in the liquid and glass phases, we find that icosahedra dominate the local order in metallic glasses, with $l \sim 0.85$ most favoring the formation of icosahedral clusters. Finally, phase separation is observed as l decreases. The onset of phase separation is $l \sim 0.75$ for the binary system and $l \sim 0.80$ for the ternary system. Section 3.2 outlines the methods and computational details while the rest reports the results and discussions.

3.2 Simulation methods

To determine the effect of atomic size ratio on the glass transition and crystallization, we changed only the lattice parameter a of the Cu atoms. This leads to the introduction of the new atoms Cu^{*} and Cu^{**}, which have the same e, c, n and m force field parameters as Cu (see chapter 1). The final size parameters for Cu^{*} and Cu^{**} are given in Table 3-1. Note that the l parameter is the size ratio of adjacent sized atoms, for example, Cu^{*} to Cu^{**} in the binary system and Cu^{*} to Cu or Cu to Cu^{**} in the ternary system. The binary system is composed of 50% Cu^{*} atoms and 50% Cu^{**} atoms with size ratio $l = a_{Cu^{*}} / a_{Cu^{**}}$ while the ternary system is composed of $1/3 Cu^{*}$, 1/3Cu and $1/3 Cu^{**}$ with size ratio $l = a_{Cu^{*}} / a_{Cu} = a_{Cu} / a_{Cu^{**}}$.

The MD simulations were performed using systems with 500 atoms per periodic cell. For the ternary system we used 167 Cu^{*} and Cu^{**} atoms and 166 Cu atoms. We used the Parinello-Rahman-Hoover formalism to describe constant temperature, constant

stress (*TtN*) conditions (Parrinello and Rahman, 1980; Hoover, 1985; Ray and Rahman, 1985). The integration step is chosen to be 1fs for both high and low temperature simulations.

To generate the liquid phase for each alloys, we started with a FCC lattice of Cu^{**} (large atom) and randomly substituted the smaller atoms (Cu^{*} and Cu). This procedure minimizes the disturbances such as strain energy caused by the size mismatch. Next, we equilibrated this alloy for 50psec with *TtN* dynamics at T=300K and zero pressure to obtain the starting density. This was followed by a heating cycle in which the system was heated from 300K to 1600K in increments of 100K for 25psec. We found that all systems melted below 1400K, but we continued to heat to 1600K to ensure a well equilibrated melt. The cooling cycle consisted of a similar sequence in which we cooled the sample to 300K in decrements of 100K for 25ps.

3.3 Heating-cooling cycles for $Cu^{*}_{50}Cu^{**}_{50}$ with l =1.0

In Fig. 3-1, a single heating-cooling cycle is shown for the binary $Cu^{*}_{50}Cu^{**}_{50}$ system with l=1.0. This represents the special case in which all atoms are identical to Cu. This system is melted by increasing the temperature in 100K increments and equilibrating for 25psec at each temperature, corresponding to a heating rate of 4×10^{12} K/sec. The sharp discontinuity in the volume (Fig. 3-1(a)) between T=1200K and 1400K provides an initial estimate of the melting temperature. To obtain a more precise estimate for the melting temperature while maintaining the same heating rate, the temperature increment is reduced to 20K and the time step is decreased to 5psec. The resulting change in volume versus as a function of temperature shows a distinct rise in volume

(first order phase transition), corresponding to a melting temperature of T_m=1360K ± 10K (Fig. 3-1(a)). This agrees with the experimentally determined melting temperature T_m=1358K for pure Cu (Kittel, 1996).

Crystallization occurs during the cooling cycle at T_x=650K ± 50K (Fig. 3-1(a)). This is far below the T_m due to the very rapid cooling rate, 4×10^{12} K/s, which leads to considerable supercooling. By examining the radial distribution function (RDF) at 300K, it is determined that the final state of the quenched sample is a crystal (Fig. 3-1(b)). For the starting alloy at 300K, the RDF shows the peaks of a FCC structure at s, $\sqrt{2}s$, $\sqrt{3}s$, $2s$, $\sqrt{5}s$, $\sqrt{6}s$, $\sqrt{7}s$, where s is the first nearest neighbor distance. In the liquid phase at 1600K these secondary peaks are gone. However, the quenched structure shows that the FCC pattern is almost recovered. Here, the maxima in the third and higher peaks are reduced somewhat, but their positions remain the same. This reduction occurs because the cooled crystal at 300K is not a perfect FCC structure compared to the starting structure. This will be discussed in detail in section 3.5.2.

A most sensitive measure of the phase transition (to glass or crystal) is provided by extracting the Wendt-Abraham (WA) parameter from the RDF (Wendt and Abraham, 1978). The Wendt-Abraham parameter is defined by $R^{WA}=g_{min}/g_{max}$, where g_{min} and g_{max} are the magnitudes of the first minimum and first maximum of the RDF. As shown in Fig. 3-1(c), the temperature dependence of R^{WA} changes in both magnitude and slope at crystallization.

3.4 Heating-cooling cycles for $Cu^{*}_{50}Cu^{**}_{50}$ with λ=0.9

The same heating and cooling procedure was performed for l values down to 0.5. When l=0.90, the melting occurs at T_m=1140K$\pm$10K (Fig. 3-2(a)) that is 220K lower than for l=1.00. We attribute this decrease in T_m to the strain energy filed generated by the non-equivalent atomic sizes. Upon cooling, the volume exhibits only subtle changes at the glass transition temperature. Unlike crystallization, there is no dramatic drop in the volume at the glass transition. However, there is a change in the RDF, as shown in Fig. 3-2(b). The RDF of cooling simulation at T=300K retains the overall shape of the liquid phase. In dramatic contrast with the l=1.0 case, the peak at $\sqrt{2}s$ is completely absent. This peak exists only in atoms belong to two adjacent closest packed planes in the FCC or HCP structures. In addition, the RDF does show a split in the second peak. This split is indicative of amorphous atomic packing and is observed experimentally in all metallic glasses, but not in liquids (Finney, 1977).

The temperature dependence of the Wendt-Abraham parameter R^{WA} leads to a clear intersection between two straight lines at T_g=470K$\pm$12K, which indicates the structural arrest by the glass transition. Additional evidence of glass transition can be found in transport properties, such as diffusivity. The temperature dependence of the diffusivity shows a break around the glass transition temperature. Previously, we have measured diffusivity as a function of temperature and confirmed a glass transition (H.-J. Lee, 2001). These studies of melting, crystallization, and the glass transition all as a function of l provide material expected to be useful in understanding the thermodynamics of these systems.

3.5 Structural properties

3.5.1 The Honeycutt-Andersen (HA) index

Glasses have no long-range order, making it difficult to analyze their structure. For such systems, a very useful assessment of local structure is provided by a Honeycutt and Andersen (HA) analysis (Honeycutt and Andersen, 1987). In this framework, the local structure is classified using a sequence of four integers (*ijkl*), where:

1. The first integer *i* is 1 when the atoms in the root pair are bonded, otherwise it is 2,
2. The second integer *j* is the number of nearest atoms shared with the root pair,
3. The third integer *k* is the number of nearest-neighbor bonds among the shared neighbors,
4. The fourth integer *l* provides additional information about nearest-neighbor bond geometry.

The first minimum in the partial radial distribution function (PRDF) is used as the cutoff distance in determining whether atoms are bonded or not. Since the atoms have different sizes, we separately analyze all three combinations of pairs in the $Cu^{*}_{50}Cu^{**}_{50}$ binary system (Cu^{*}-Cu^{*}, Cu^{**}-Cu^{**}, and Cu^{*}-Cu^{**}), leading to three different cutoff distances for the pair analysis. For the ternary system, this leads to a different cutoff distance for each of the six combinations of pairs.

Table III shows the HA analysis for several structures. The pair fractions shown here are normalized so that the sum over all cases for nearest neighbors (i=1) add to unity. General observations are:

- the FCC structure leads only to 1421 while
- the HCP structure leads to equal amounts of 1421 and 1422
- A simple icosahedron (ICO-13) has 71% 1321 and 29% 1551 (also 71 % 2331) while

- the larger icosahedral structures (ICO-55) lead to significant amounts of 1422 (but not 1421), increased amounts of 1311, with decreases in 1321, 1551, and 2331.
- Large icosahedra such as ICO-309 lead to over 30% each of 1421 and 1422, with decreases in 1321, 1551, and 2331.

Thus, the 1421 and 1422 pairs are characteristic of the closest packed crystalline structures (FCC and HCP), while 1321, 1551, and 2331 pairs are characteristics of icosahedral ordering.

3.5.2 HA analysis of heating and cooling $Cu^{*}_{50}Cu^{**}_{50}$ with l =1.0

Fig. 3-3(a) shows the HA pairs as a function of temperature as the binary $Cu^{*}_{50}Cu^{**}_{50}$ system with l=1.0 is heated from 300K to 1600K. To reduce the statistical error of this analysis, we sampled 200 configurations uniformly separated over 20ps and averaged the HA pair analysis results at each temperature. The system starts as a single FCC crystal at T=300K, leading only to 1421 pairs. As the temperature increases, the 1421 pair fraction decreases smoothly then remains constant in the liquid phase. The 2331 pairs increase rapidly with temperature. After the temperature increases further from T_m, the 2331 pairs decrease slowly, indicating the loss of local order in liquid. The 1551 pairs follow the behavior of 2331, but less dramatically. The 1422 characteristic of HCP increases slowly up to T_m and then remains constant, nearly twice the value of 1421.

In the cooling simulation (Fig 3-3(b)), the 1551 and 2331 pairs increase uniformly as the system supercools, and then decrease abruptly upon crystallization. Here 1551 drops to zero while 2331 drops to a constant value of 0.13. Simultaneously, the 1421 and 1422 pairs remain almost constant in the liquid and supercooled liquid regime, but

increase rapidly upon crystallization. The final values after crystallization are 0.62 for 1421 and 0.29 for 1422, indicating that the crystallized sample has mostly FCC and HCP phases. The coexistence of FCC and HCP in a quenched pure Cu system has been observed previously in MD simulations (Liu *et al.*, 2001). It is mostly these HCP phases that lead to 2331 pairs in the quenched sample after crystallization. The 1.02% increase in volume at T=300K (Fig. 3-1(a)) from the heating and cooling runs is also due to the formation of a non-FCC phase, such as HCP.

These results demonstrate that the 1551 and 2331 pairs are strongly correlated, while the 1421 and 1422 pairs are anti-correlated with respect to the 1551 and 2331 pairs. This suggests the existence of two major competing local orders:

- close packed FCC/HCP ordering (1421 and 1422 pairs) and
- icosahedral ordering (1551 and 2331 pairs).

3.5.3 HA analysis of heating and cooling $Cu^{*}_{50}Cu^{*}_{50}$ with λ=0.9

For the binary system with λ=0.90, the heating simulation (Fig. 3-4(a)) shows a more rapid decrease in 1421 pairs than for λ=1.0. As for the pure crystal, the 2331 pairs increase rapidly to 0.37 just below melting, jumping to 0.72 by 1200K (just above melting) and then drops with increasing temperature. Similarly, the icosahedral 1551 jumps from 0.03 just below melting to 0.20 by 1200K and then drops with increasing temperature. In the melt, the 1422 pair remains constant at 0.06, just as for pure Cu.

In the cooling simulation, the 1551 and 2331 pairs increase as the temperature decreases until a maximum at 400K of 0.97 for 2331 and 0.35 for 1551 is reached. Both

cases seem to show a bigger increase between 700K and 600K but this is not reflected in the WA analysis (Fig. 3-2(c)).

In contrast with the l=1.0 case, the 1421 and 1422 pairs remain almost constant at 0.03 and 0.05, respectively. The preference for 1422 over 1421 in the liquid or glass phase is characteristic of icosahedral clusters where Table III shows that neither occurs for ICO-13, but 1422 is 38 % for ICO-55 and 39% for ICO-147, while 1421 is 0% and 17%, respectively.

Fig. 3-5 shows the HA analysis as a function of l for samples cooled to 300K for the binary and ternary systems (again quenched from 1600K using a $4x10^{12}$ K/s cooling rate). For l>0.95 and higher, the system becomes a FCC/HCP crystal upon cooling, showing almost no 1551 pair character. For l=0.95 and lower, the system becomes a glass upon cooling, leading to large fractions of the 1551 and 2331 pairs. The binary system leads to 2331 over 90% and 1551 over 30% for l=0.6 to 0.9. The threshold size ratio for crystallization and glass transition appears to be between l=0.95 and 1.00. In the ternary system, the 1551 and 2331 pairs show a distinct maximum at l~0.85 while the binary system shows a maximum at 0.85 for 2331 but is rather flat for 1551. For the binary system the 1551 and 2331 pairs decreases abruptly below l=0.60 while the 1421 and 1422 pairs increase, implying partial crystallization. The ternary system shows more complicated behavior, with a local minimum at l~0.80 in the 1551 and 2331 pair fractions. These phenomena are discussed in more detail in section 3.4. We should point out that these observations are for quite fast quenching rates of $4x10^{12}$ K/sec, well beyond the fastest available experimentally, 10^6 K/sec. Probably lower quenching rates would

have extended the range for forming the crystalline phase to values lower than the l=0.95 observed here.

3.5.4. Coordination polyhedra analysis

The coordination polyhedron of an atom is formed by connecting the centers of atoms in the first nearest neighbor shell with lines. According to this definition, the coordination polyhedra present in the FCC and HCP structures have the shapes of cubo-octahedron (CN_FCC) and twinned cubo-octahedron (CN_HCP) respectively (William Hume-Rothery, 1969). Both have coordination number (CN) 12, which is the highest possible CN for a packing of uniformly sized spheres. In complex structures, a third kind of coordination polyhedra, which also has CN 12, is present. This is an icosahedron (CN12), which is found in many of the complex crystal structures of transition metal alloys, including the s phase and the $a-$manganese structures (William Hume-Rothery, 1969). However, there is no space-filling structure made up of icosahedra alone due to the five-fold axis of symmetry present in an icosahedron. To have large portion of CN12 in structure, Frank and Kasper proposed that higher coordination polyhedra, such as CN14, CN15 or CN16, must be present in complex crystal structures (Frank and Kasper, 1958).

Among Frank-Kasper polyhedra, CN12 is often observed experimentally in diffraction patterns of melt-spun metallic glasses (Saida *et al.*, 2000). Considering metallic glasses have topologically close packed structures, the randomly packed icosahedra with some CN14, CN15, and CN16 may be an appropriate structure of metallic glasses. To clarify the role of local icosahedral ordering and the possible role of

other Frank-Kasper polyhedra in glasses, we have analyzed the coordination polyhedra for the binary and ternary systems.

Table 3-3 summarizes the geometrical characteristics of various coordination polyhedra, including their HA pair representations. These characteristics can be used to identify the type of coordination polyhedra present in each sample. For the glass phases (l=0.6 to 0.9), we find many (ranging from 19 to 35 out of total 500) CN12 polyhedra with one or two CN14, CN15, and CN16 polyhedra but one or zero CN_FCC and CN_HCP. Therefore, we focus on CN12 in analyzing the coordination polyhedra of glasses.

The bars in Fig 3-6(a) show the percentage of CN12 atoms as a function of l for the binary $Cu^{*}_{50}Cu^{*}_{50}$ system after cooling to T=300K. The percentage is 4 to 7 % for l=0.6 to 0.9, where essentially all of these icosahedra have the smaller atom Cu^{*} at the center (dark bars). The total number of atoms in these icosahedra (central plus 12 surface atoms) is also shown. This peaks at 50% for l=0.8 and is generally above 30% for l=0.6 to 0.9. We note that for l=0.8, the fractions of Cu^{*} and Cu^{**} atoms in the icosahedra is equal but, for l=0.65, there is very distinct fractionalization of the system, so that mostly only the smaller atoms are associated with icosahedra. This implies heterogeneity in the microstructure (vide infra).

The results for the ternary system are shown in Fig. 3-6(b). Here, we see a maximum of CN12 atoms at l=0.87. The majority of CN12 atoms are the smallest ones, Cu^{*}, with the remainder being the intermediate size, Cu. The total number of atoms in these icosahedra (central plus 12 surface atoms) is also shown. This peaks at 50% for l=0.87 and is above 37% for l=0.87 to 0.92. We note that for l=0.8 the fractions of Cu^{*}

and Cu^{**} atoms in the icosahedra are equal but, for l=0.74, there is very distinct fractionalization of the system so that mostly only the smaller atoms are associated with icosahedra with very few of the largest. This implies heterogeneity in the microstructure (vide infra). The bimodal behavior in Fig. 3-6(b) of icosahedral fraction parallels the behavior in the 1551 and 2331 pairs observed in Fig. 3-5(b), confirming that these are measuring similar features.

As demonstrated in Fig. 3-6, the smaller atom is often observed as the center of icosahedra and the maximum number of icosahera is observed at l=0.80 in binary system and at l=0.87 for the ternary system. To analyze the origin of this phenomenon, a single icosahedron cluster is made with the small atom (Cu^{*}) at the center position and the 12 large atoms (Cu^{**}) at the surface. Fig. 3-7 shows the potential energies of the icosahedron as a function of the atomic size ratio l at T=0K? We find that the minimum potential energy for the 13-atoms icosahedron occurs at l~0.84. It should be noted that this analysis considers only the 13 atoms of a single, isolated icosahedron. Therefore, the surface atoms have only 6 bonds and the ratio of Cu^{*} to Cu^{**} is 1:12 instead of 1:1. However, this simple analysis is helpful in understanding the strong preference for icosahedral structures at l~0.85 and the preference for Cu^{*} as the icosahedral center atoms (CN12).

3.5.5 Analysis of topological connects

Fig. 3-8 illustrates the three-dimensional topology of the icosahedral atoms. The $Cu^{*}_{50}Cu^{**}_{50}$ system with l=0.85 is shown in Fig. 3-8(a)-(d). The center of the CN12 icosahedra are shown as dark balls which are connected by solid lines when they share

atoms in their first coordination shell. The atoms in the CN12 coordination shell are shown as light balls.

Fig. 3-8(a) and 8(b) show snapshots at T=800K (above the glass transition) separated by 19.9psec. Here, we see somewhat similar structural patterns, but with different atoms. This suggests that above the glass temperature there are fewer icosahedron atoms (average over 20psec simulation gives 5 atoms out of 500 atoms) and that the icosahedral domains are dynamic and fluctuating

Fig. 3-8(c) and 3-8(d) show the same system at T=300K, well below the glass transition temperatures, separated by 19.9psec. There are more icosahedron atoms (45.2%, see Fig. 3-6(a)) and the icosahedral domains persist throughout the simulation at T=300K.

These results combined with the temperature dependence of the icosahedral pairs (1551 and 2331) in Fig. 3-4(b), the correspondence between the l dependences of these pairs (Fig. 3-5(a)), and the CN12 analysis (Fig. 3-6(a)) suggests the following pictures. For temperatures above the T_g, decreasing temperature leads to increased numbers of CN12 centers, which at higher temperatures are ephemeral and not highly connected (as in Fig. 3-8(a)(b)). As these icosahedral domains grow with decreasing temperature they interconnect, which slows the dynamic variations. At some point, the interlocking of these domains is sufficient (perhaps when the interconnections become infinite, *i.e.*, when they percolate) so that the domain structure remains constant. This may correspond to the glass transition temperature. If so, this may be very similar to the formation of glassy or amorphous phases in polymers (Zallen, 1998). The $Cu^{*}_{33.3}Cu_{33.3}Cu^{**}_{33.3}$ system with

l=0.87 is shown in Fig. 3-8(e) for 300K. Here we see interlocking icosahedral domains much as in Fig. 3-8(c)(d) for the binary case, suggesting a similar picture.

3.6 Phase separation

3.6.1 Binary system

Fig. 3-9(a) shows the quenched structure at 300K for the binary $Cu^{*}_{50}Cu^{**}_{50}$ system with l=0.50. Here, it is quite clear that there are two separate phases (Cu^{*} phase and Cu^{**} phase) with a well-defined phase boundary. The Cu^{*} and Cu^{**} phases are almost pure with a well-defined phase boundary.

In Fig. 3-9(a) the Cu^{*} phase appears to be disordered while the Cu^{**} phase appears to be ordered. This is made more quantitative in Fig. 3-9(b) showing the Cu^{*}-Cu^{*} pair RDF (PRDF) in the liquid phase (1600K) and upon cooling to 300K. This shows that the Cu^{*} has become a glass (second peak at 0.33 nm is split just as in Fig. 3-2(b)), but there is a small amount of close packed crystalline character (the small bump at $r = \sqrt{2}s$, as in Fig. 3-1(b)). Also, the HA analysis on the Cu^{*} phase gives pair fraction values of 0.13 for 1421 pairs, 0.13 for 1422 pairs, 0.09 for 1551 pairs, and 0.48 for 2331 pairs, indicating the coexistence of crystalline and glass structures.

On the other hand, the PRDF of the Cu^{**} phase in Fig. 3-9(c) shows a clear crystalline character. In addition, the HA analysis on this Cu^{**} phase gives pair fraction values of 0.38 for 1421 pairs, 0.41 for 1422 pairs, 0.02 for 1551 pairs, and 0.10 for 2331 pairs. Again, this indicates crystalline character. Given that the Cu^{**} atoms have crystallized, we speculate that the lack of crystallizing of the Cu^{*} may be because the

atomic size ratio effect on the interface per unit volume is bigger in the Cu^{*} phase when combined with rapid quenching.

To further quantify this phase separation behavior, Fig. 3-10 shows the pair fraction (defined as the number of a specific pair type present in the sample normalized by the total number of pairs in the system) after quenching at T=300K as a function of l. For a binary system with l=1.0, a random alloy should give 0.25 for like pairs (Cu^{*}-Cu^{*} and Cu^{**}-Cu^{**}) and 0.50 for unlike pairs (Cu^{*}-Cu^{**}), which is very close to the observed values in Fig. 3-10. As l decreases, the fraction of unlike pairs decreases while the fraction of Cu^{**}-Cu^{**} pairs increases. This is due to the phase separation between different atomic species. The decrease of the unlike pair fraction becomes abrupt at l~0.75, indicating the existence of a threshold l for phase separation.

Finally, the phase separation behavior is closely related to the number of icosahedral atoms present. At the onset of phase separation, the icosahedral character shows a local minimum and the concentrations of each atom in icosahedra start to change noticeably. In the $Cu^{*}_{50}Cu^{**}_{50}$ system, a hint of this phase separation occurs at l~0.75, where the number of icosahedral atoms and the total number of atoms in icosahedra show a local minimum (Fig. 3-6(a)). In addition, the concentration of Cu^{*} and Cu^{**} atoms in icosahedra start to change rapidly below l~0.75.

3.6.2 Ternary system

As shown in Fig. 3-11(a), ternary systems show an even more pronounced phase separation behavior among Cu^{*}, Cu, and Cu^{**} at l=0.55. Here, we see a strong phase separation between the smallest (Cu^{*}) and the largest (Cu^{**}) atoms, with the intermediate

size (Cu) forming an interfacial layer between the two phases. This is because the size ratio of Cu^{*} to Cu^{**} is 0.30 when the Cu^{*} to Cu and Cu to Cu^{**} ratios are 0.55 (Table 3-1). Therefore, it is favorable to make Cu^{*}/Cu and Cu/Cu^{**} interfaces, rather than a Cu^{*}/Cu^{**} interface, to accommodate the size ratio induced phase separation. The separated Cu^{*}, Cu, and Cu^{**} phases become either glass or crystal, depending on the magnitude of the size ratio and the phase separation. The Cu^{**}-Cu^{**} PRDF in Fig. 3-11(d) shows that the Cu^{**} phase in Fig. 3-11(a) is crystalline. However the PRDF in Fig. 3-11(b) for Cu^{*}-Cu^{*} and in Fig. 3-11(c) for Cu-Cu indicate that these phases are disordered (glasses).

Fig. 3-12 shows the pair fraction for the ternary systems after quenching to T=300K. The ternary system also demonstrates phase separation among Cu^{*}, Cu, and Cu^{**} as l decreases (like pairs in Fig. 3-12(a) and unlike pairs in Fig. 3-12(b)). In particular, the Cu^{*}-Cu^{**} pair fraction decreases rapidly at $l \sim 0.8$ and becomes almost zero at $\lambda < 0.7$. This implies that Cu^{*} and Cu^{**} have nearly no contact at $l < 0.7$, which is made possible by having the Cu layer between the Cu^{*} phase and the Cu^{**} phase (Fig. 3-11(a)). It should be noted that ternary systems also have the maximum icosahedral character (Fig. 3-5(b) and Fig. 3-6(b)) at the onset of phase separation ($l \sim 0.8$) and the concentration of Cu^{**} atoms in icosahedra start to decrease rapidly at $l \sim 0.8$.

3.7 Phase diagram

The phase diagram provides important information in controlling crystallization and phase separations. Several methods have been developed and used to calculate phase diagrams using MD or MC simulations using the hard sphere model or LJ potential (Laird and Haymet, 1992; Eldridge *et al.*, 1993; Kofke, 1993; Cottin and Monson, 1995;

Hitchcock and Hall, 1999). In particular, Hitchcock and Hall describe how the size ratio and the potential well depth ratio change the phase diagram in the model LJ mixtures (1999). Although they used the LJ potential, we think that the phase diagrams of model LJ systems would be similar to the phase diagrams of model many-body potential systems. Some general properties, such as the melting point as a function of size ratio, agree with the phase diagram from LJ systems (see Chapter 2).

At the potential well depth ratio 1.0, Hitchcock and Hall show that the phase diagram changes from azeotrope to eutectic as the size ratio decreases (Hitchcock and Hall, 1999). The size ratio that separates the transition from azeotrope to eutectic is l~0.85, which coincides with the size ratio at the maximum icosahedral character from this work. Since the glass is more easily formed at the eutectic point, it is possible that the local icosahedral order is indicative of the glass forming ability.

In addition to the size ratio, it would be interesting to study the potential well depth ratio effect on the glass forming ability. Previously, we observed phase separation at l=0.5 and potential well-depth ratio=1.0, but we saw the NaCl structure at l=0.5 and potential well-depth ratio=0.125 (Lee, in press). This suggests that structural properties, such as phase separation behavior and inter-metallic compound formation, is a function of λ and the potential well-depth ratio.

3.8 Conclusions

To investigate phase transitions in glass forming liquids we carried out molecular dynamics simulations using the Q-SC many-body force field as a function of the atomic

size ratio ($l \leq 1.0$). We find three regimes of phase behavior, defined by the magnitude of the size ratio l.

- When $0.95 < l \leq 1.0$, crystallization occurs easily upon cooling.
- As l decreases, we find glass formation.
- As l decreases further, we observe phase separation rather than glass formation.

Using Honeycutt-Anderson pair index analysis and coordination polyhedral analysis, we find that icosahedra dominate the local order in metallic glasses, with $l \sim 0.85$ most favoring the formation of icosahedral clusters.

References

Cottin, X., and Monson, P.A. (1995). Substitutionally Ordered Solid-Solutions of Hard-Spheres. J. Chem. Phys. *102*, 3354-3360.

Egami, T., and Waseda, Y. (1984). Atomic Size Effect on the Formability of Metallic Glasses. J. Non-Cryst. Solids *64*, 113-134.

Eldridge, M. D., Madden, P.A., and Frenkel, D. (1993). Entropy-Driven Formation of a Superlattice in a Hard-Sphere Binary Mixture. Nature *365*, 35-37.

Finney, J.L. (1977). Modeling Structures of Amorphous Metals and Alloys. Nature *266*, 309-314.

Frank, F.C., and Kasper, J.S. (1958). Complex Alloy Structures Regarded as Sphere Packings .1. Definitions and Basic Principles. Acta Crystallographica *11*, 184-190.

H.-J. Lee, Y.Q., A. Strachan, T. Cagin, W. A. Goddard III, W. L. Johnson. (2001). Molecular dynamics simulations of supercooled liquid metals and glasses. In: Mat. Res. Soc. Symp. Proc., vol. 644, ed. A.R.Y. Akihisa Inoue, William L. Johnson and Reinhold H. Dauskardt, Boston: Mateirals Research Society, L2.3.1.

Hitchcock, M.R., and Hall, C.K. (1999). Solid-liquid phase equilibrium for binary Lennard-Jones mixtures. J. Chem. Phys. *110*, 11433-11444.

Honeycutt, J.D., and Andersen, H.C. (1987). Molecular-Dynamics Study of Melting and Freezing of Small Lennard-Jones Clusters. J. Phys. Chem. *91*, 4950-4963.

Hoover, W.G. (1985). Canonical Dynamics - Equilibrium Phase-Space Distributions. Phys. Rev. A *31*, 1695-1697.

Johnson, W.L. (1998). Bulk glass-forming metallic alloys: science and technology. In: Mat. Res. Soc. Symp. Proc., vol. 554, ed. A.I.a.C.T.L. William L. Johnson, Boston, MA: Mateirals Research Society, 311.

Kittel, C. (1996). Introduction to solid state physics. John Wiley & Sons, Inc.

Kofke, D.A. (1993). Gibbs-Duhem Integration - a New Method for Direct Evaluation of Phase Coexistence by Molecular Simulation. Mol. Phys. *78*, 1331-1336.

Laird, B.B., and Haymet, A.D.J. (1992). Phase-Diagram for the Inverse 6th-Power Potential System from Molecular-Dynamics Computer-Simulation. Mol. Phys. *75*, 71-80.

Lee, H.-J., Cagin, T., Goddard, W. A., Johnson, W. L. (in press). Molecular dynamics simulations of glass formation and crystallization in binary liquid metals. Materials Science Forum *in press.*

Liu, C.S., Xia, J.C., Zhu, Z.G., and Sun, D.Y. (2001). The cooling rate dependence of crystallization for liquid copper: A molecular dynamics study. J. Chem. Phys. *114*, 7506-7512.

Parrinello, M., and Rahman, A. (1980). Crystal-Structure and Pair Potentials - a Molecular-Dynamics Study. Phys. Rev. Lett. *45*, 1196-1199.

Qi, Y., Cagin, T., Kimura, Y., and Goddard, W.A. (1999). Molecular-dynamics simulations of glass formation and crystallization in binary liquid metals: Cu-Ag and Cu-Ni. Phys. Rev. B *59*, 3527-3533.

Ray, J.R., and Rahman, A. (1985). Statistical Ensembles and Molecular-Dynamics Studies of Anisotropic Solids .2. J. Chem. Phys. *82*, 4243-4247.

Saida, J., Matsushita, M., Li, C., and Inoue, A. (2000). Formation of icosahedral quasicrystalline phase in Zr70Ni10M20(M=Pd, Au, Pt) ternary metallic glasses. Appl. Phys. Lett. *76*, 3558-3560.

Sutton, A.P., and Chen, J. (1990). Long-Range Finnis Sinclair Potentials. Philos. Mag. Lett. *61*, 139-146.

Wendt, H.R., and Abraham, F.F. (1978). Empirical Criterion for Glass-Transition Region Based on Monte- Carlo Simulations. Phys. Rev. Lett. *41*, 1244-1246.

William Hume-Rothery, R.E.S.a.C.W.H. (1969). The structure of metals and alloys. The institute of metals.

Zallen, R. (1998). The Physics of Amorphous Solids. A Wiley-Interscience Publication.

Table 3-1. Atom size parameters for the binary and ternary model alloy systems. The parameter l is defined as the size ratio of Cu^{*} to Cu^{**} in the binary system and Cu^{*} to Cu and Cu to Cu^{**} in the ternary system. These size parameters were chosen to keep constant the geometric mean of the size parameters for Cu^{*} and Cu^{**}, $a_{ij} = \sqrt{a_{ii} a_{jj}}$.

(a) Binary system

l	Cu^{*}	Cu^{**}
0.50	2.54771	5.09541
0.55	2.67206	4.85828
0.60	2.79087	4.65145
0.65	2.90483	4.46897
0.70	3.01449	4.30641
0.75	3.12029	4.16039
0.80	3.22262	4.02828
0.85	3.32180	3.90800
0.90	3.41811	3.79790
0.95	3.51177	3.69660
1.00	3.60300	3.60300

(b) Ternary system

l	Cu^{*}	Cu	Cu^{**}
0.50	1.80150	3.60300	7.20600
0.55	1.98165	3.60300	6.55091
0.60	2.16180	3.60300	6.00500
0.65	2.34195	3.60300	5.54308
0.70711	2.54771	3.60300	5.09541
0.74162	2.67206	3.60300	4.85828
0.77460	2.79087	3.60300	4.65145
0.80623	2.90483	3.60300	4.46897
0.83666	3.01449	3.60300	4.30641
0.86603	3.12029	3.60300	4.16039
0.89443	3.22262	3.60300	4.02828
0.92195	3.32180	3.60300	3.90800
0.94868	3.41811	3.60300	3.79790
0.97468	3.51177	3.60300	3.69660
1.00	3.60300	3.60300	3.60300

Table 3-2. Honeycutt-Andersen (HA) pair fractions for several reference systems. Here, FCC and HCP denotes bulk systems while ICO-N denotes an icosahedral clusters with N atoms. Thus, ICO_13 is a 13-atom icosahedron.

	1311	1321	1421	1422	1551	2331
FCC	0.00	0.00	1.00	0.00	0.00	0.00
HCP	0.00	0.00	0.50	0.50	0.00	0.17
ICO_13	0.00	0.71	0.00	0.00	0.29	0.71
ICO_55	0.26	0.26	0.00	0.38	0.10	0.38
ICO_147	0.26	0.13	0.17	0.39	0.05	0.26
ICO_309	0.23	0.08	0.31	0.35	0.03	0.19

Table 3-3. Coordination polyhedra

(a) Geometrical characteristcis of various polyhedra (SC is the surface coordination).

Type	CN12_FCC	CN12_HCP	CN12	CN14	CN15	CN16
Vertices						
with						
SC=4	12	12	0	0	0	0
SC=5	0	0	12	12	12	12
SC=6	0	0	0	2	3	4
Edges	24	24	30	36	39	42
Faces						
triangluar	8	8	20	24	26	28
square	6	6	0	0	0	0

(b) The number of Honeycutt-Andersen (HA) pairs in coordination polyhedra

Type	CN12_FCC	CN12_HCP	CN12	CN14	CN15	CN16
1421	12	6	0	0	0	0
1422	0	6	0	0	0	0
1551	0	0	12	12	12	12
1661	0	0	0	2	3	4

(a)

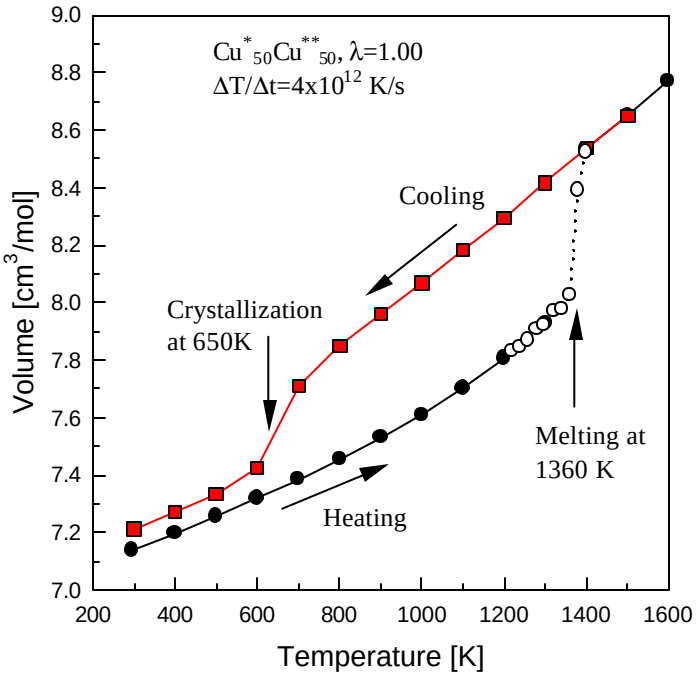
Cu*50Cu**50, λ=1.00
ΔT/Δt=4x10^12 K/s
Cooling
Crystallization
at 650K
Melting at
1360 K
Heating
Volume [cm^3/mol]
Temperature [K]
9.0
8.8
8.6
8.4
8.2
8.0
7.8
7.6
7.4
7.2
7.0
200
400
600
800
1000
1200
1400
1600

(b)

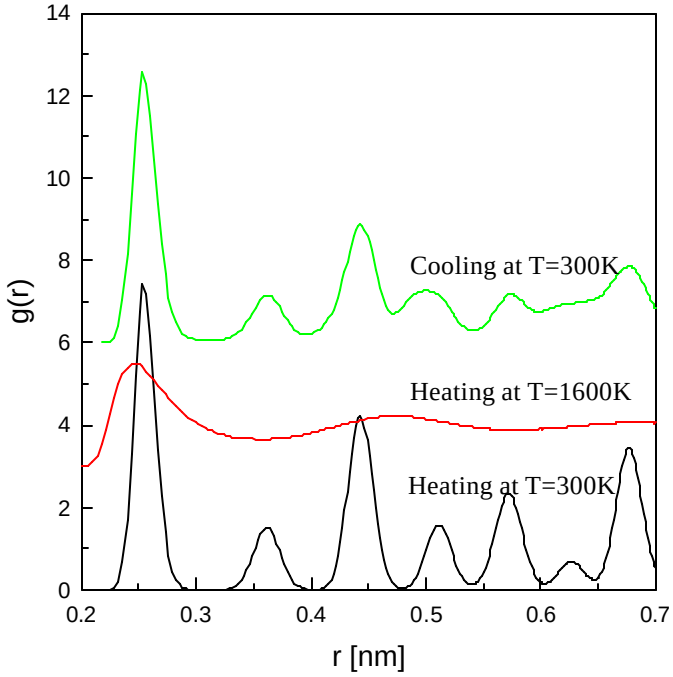
Cooling at T=300K
Heating at T=1600K
Heating at T=300K
g(r)
r [nm]
14
12
10
8
6
4
2
0
0.2
0.3
0.4
0.5
0.6
0.7

(c)

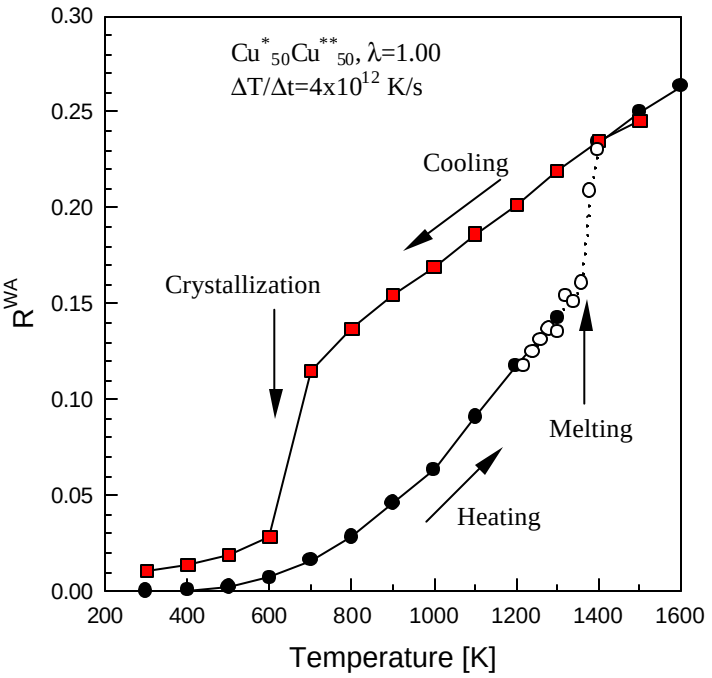

Figure 3-1. A heating and cooling cycle of $Cu^{*}_{50}Cu^{**}_{50}$ at l=1.0 with a heating/cooling rate of 100K per 25 psec ($4x10^{12}$ K/s). (a) Volume as a function of temperature. The heating run shows a melting transition at T=1360K±10K. Upon cooling, the liquid is supercooled and crystallization occurs at T=650K±50K. (b) Radial distribution functions (RDF) for three points on the heating and cooling runs; the random FCC crystal starting structure (heating at T=300K); the equilibrated liquid phase (heating at T=1600K); the crystallized systems after quenching (cooling at T=300K). (c) Wendt-Abraham parameter (R^{WA}) as a function of temperature. R^{WA} shows a discontinuity and change in slope at melting and crystallization (first order transitions), implying the dramatic change in a structural feature.

(a)

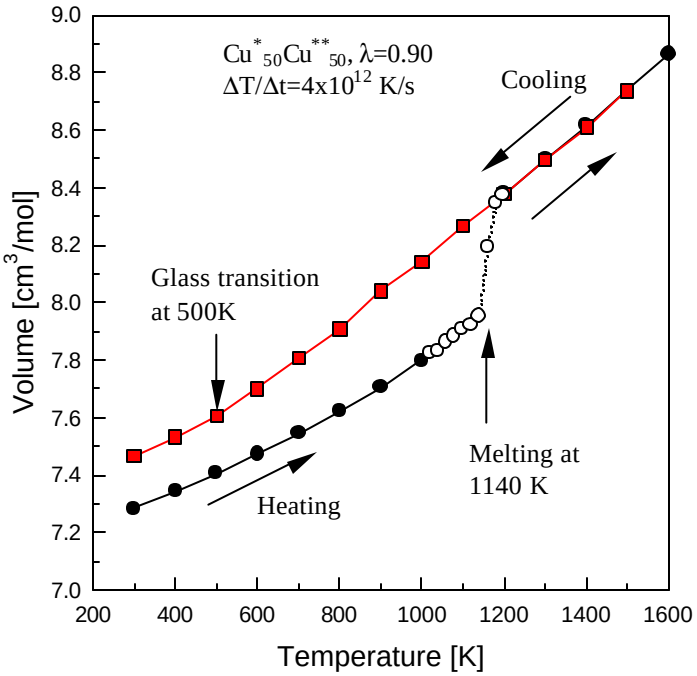
Cu*50Cu**50, λ=0.90
ΔT/Δt=4x10^12 K/s
Cooling
Glass transition
at 500K
Heating
Melting at
1140 K
Volume [cm^3/mol]
Temperature [K]
9.0
8.8
8.6
8.4
8.2
8.0
7.8
7.6
7.4
7.2
7.0
200
400
600
800
1000
1200
1400
1600

(b)

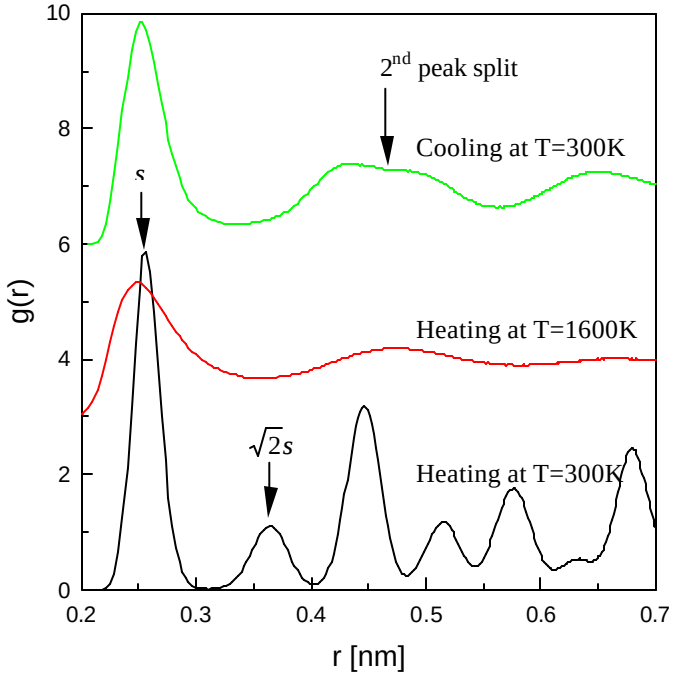
2nd peak split
Cooling at T=300K
s
Heating at T=1600K
√2s
Heating at T=300K
g(r)
r [nm]
10
8
6
4
2
0
0.2
0.3
0.4
0.5
0.6
0.7

(c)

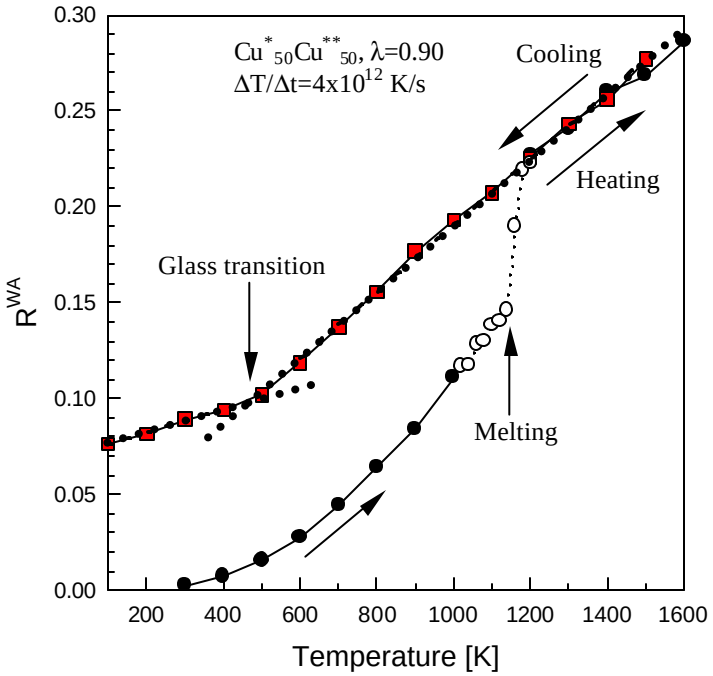

Figure 3-2. Heating and cooling cycle of $Cu^{*}_{50}Cu^{**}_{50}$ at l=0.9 with a heating/cooling rate of 100K per 25psec ($4x10^{12}$ K/s). (a) Volume as a function of temperature. Melting occurs at 1140K±10K. Upon cooling, the system transforms into a glass, but the volume curve does not provide a clear value for T_g. (b) Radial distribution function (RDF) during heating and cooling runs. Different from the starting structure (a random fcc, heating at T=300K), the RDF (cooling at T=300K) shows a bimodal splitting in a second peak, which is characteristic of amorphous atomic packing. (c) Wendt-Abraham parameter (R^{WA}) as a function of temperature. The R^{WA} changes slope at the glass transition in the cooling run. This leads to T_g=475K± 12K.

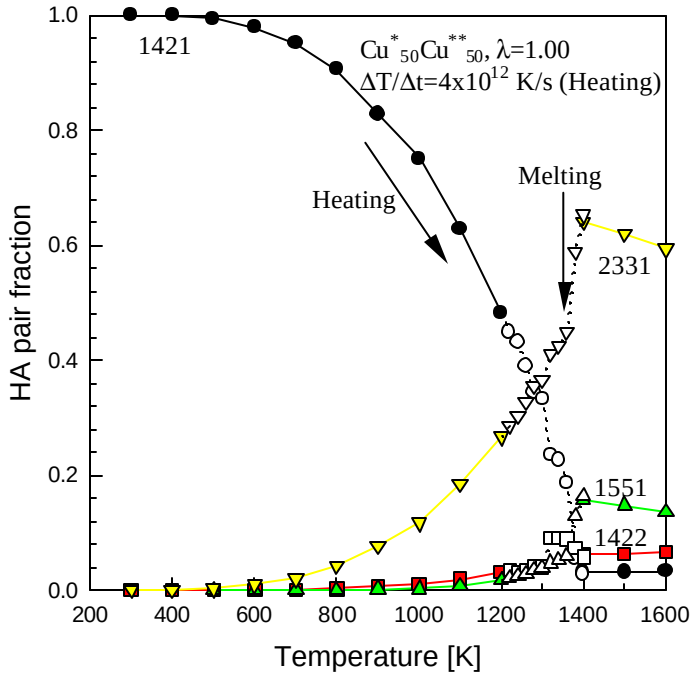

Figure 3-3(a). Honeycutt-Andersen (HA) pair fraction of heating run as a function of temperature in $Cu^{*}_{50}Cu^{**}_{50}$ at l=1.0 for a heating/cooling rate of 100K/25psec ($4x10^{12}$ K/s). Here we see that the 1421 pairs characteristic of FCC decrease gradually as the temperature increases and becomes almost constant after melting. At the same time, the 2331 and 1551 pairs increase as the temperature increases and reaches a maximum immediately after melting.

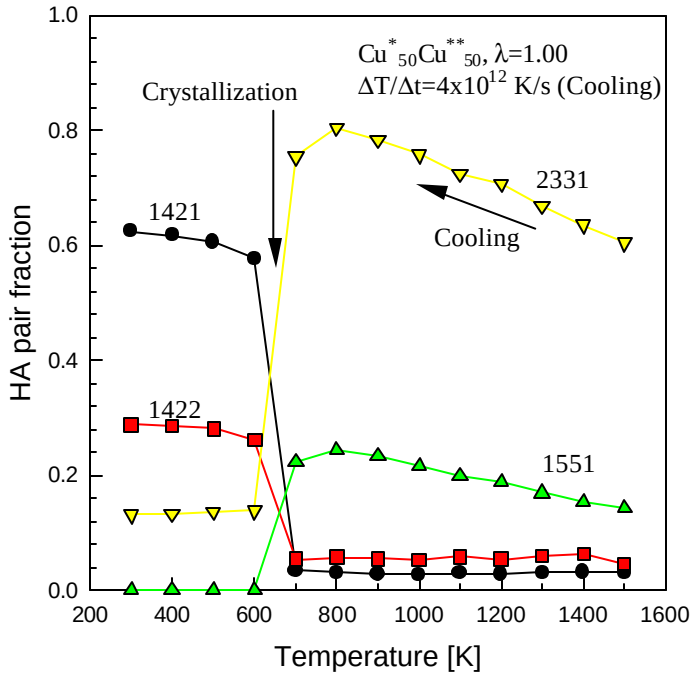

Figure 3-3(b). Honeycutt-Andersen (HA) pair fraction of cooling run as a function of temperature in $Cu^{*}_{50}Cu^{**}_{50}$ at l=1.0 for a heating/cooling rate of 100K/25psec ($4x10^{12}$ K/s). Here, the 1421 and 1422 pairs remain small and constant throughout the supercooled regime and then increase rapidly at crystallization (T=650K). Simultaneously, the 1551 and 2331 pairs increase as the liquid supercools and then decrease abruptly upon crystallization. After crystallization, the 1551 pair fraction becomes zero.

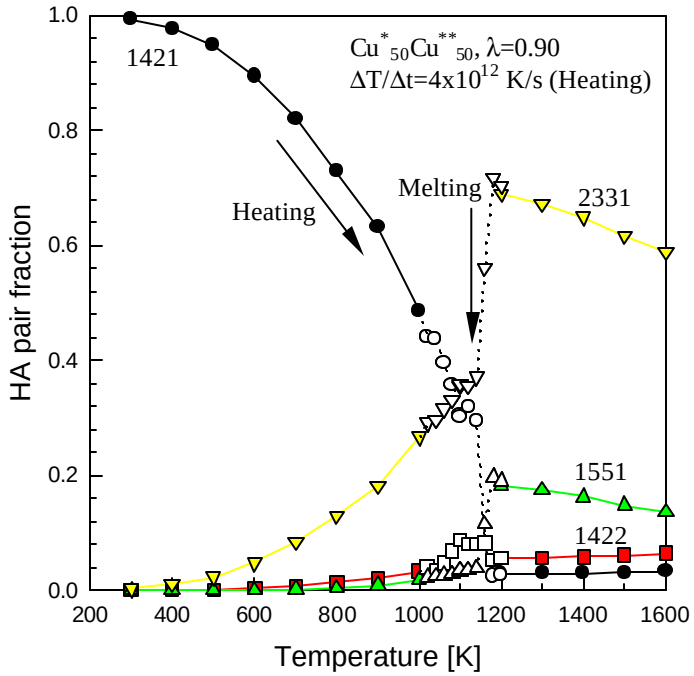

Figure 3-4(a). Honeycutt-Andersen (HA) pair fraction of heating run as a function of temperature in $Cu^{*}_{50}Cu^{**}_{50}$ at l=0.9 with a heating/cooling rate of $4x10^{12}$ K/s. Here, the 1421 pairs start to decrease much sooner than for the l=1.0 case (Fig. 3-3(a)), leading to a lower melting temperature. The 2331 and 1551 pairs increase slowly as the temperature increases, reaching a maximum immediately after melting.

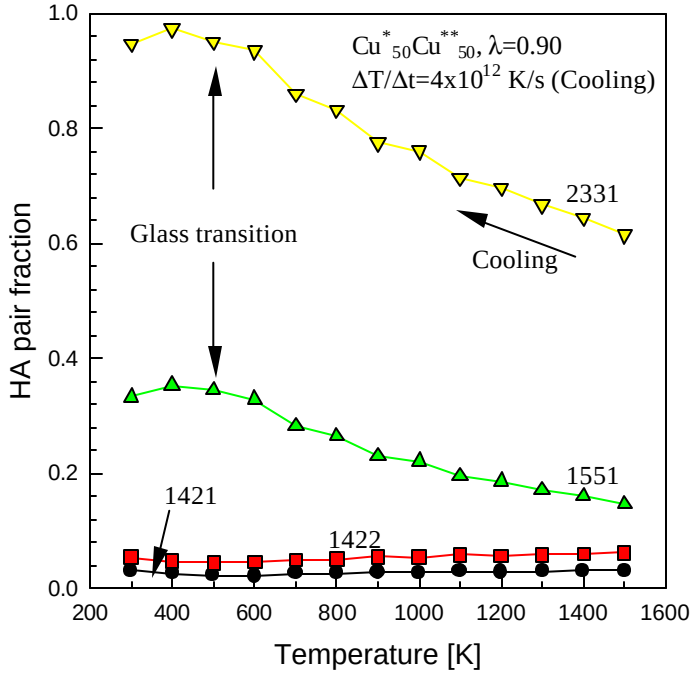

Figure 3-4(b). Honeycutt-Andersen (HA) pair fraction of cooling run as a function of temperature in $Cu^{*}_{50}Cu^{**}_{50}$ at l=0.9 with a heating/cooling rate of $4x10^{12}$ K/s. Here, the 1551 and 2331 pairs increase continuously as the temperature decreases, while the 1421 and 1422 pairs remain relatively constant throughout the run.

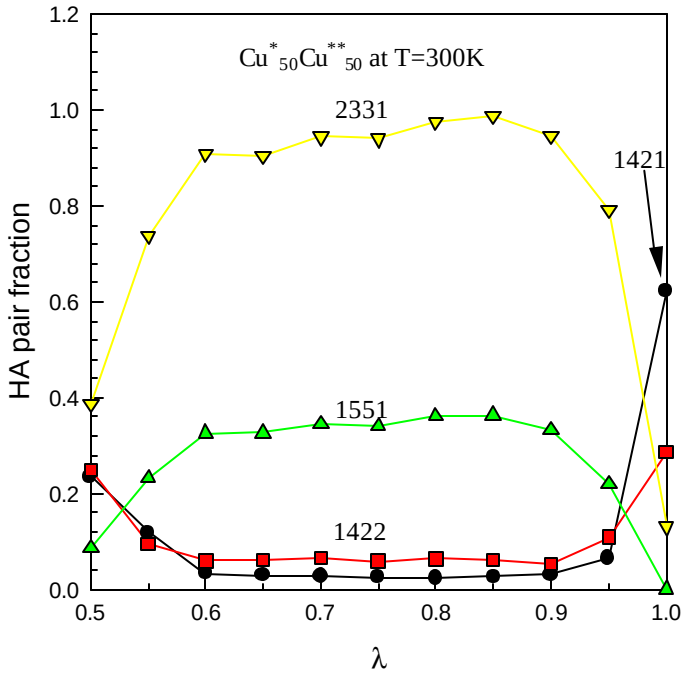

Figure 3-5(a). Honeycutt-Andersen pair fraction of binary system as a function of l at T=300K after the cooling run (cooling rate=4x10^{12} K/s). At l=1.0, the system has many 1421 and 1422 pairs and almost no 1551 pairs, indicating that it is composed of FCC and HCP phases. As l decreases, the 1551 and 2331 pairs increase dramatically, showing a maximum at l~0.85.

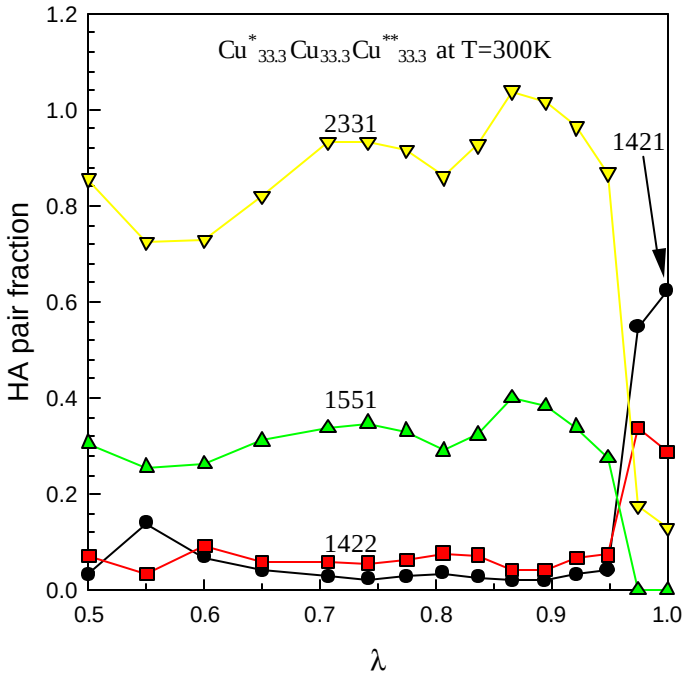

Figure 3-5(b). Honeycutt-Andersen pair fraction of ternary system as a function of l at T = 300K after the cooling run (cooling rate=$4\text{x}10^{12}$ K/s). The systems with l>0.95 crystallize, leading to large numbers of 1421 and 1422 pairs. The 1551 and 2331 pairs increase dramatically as l decreases, showing a maximum at l~0.87. However, the 1551 and 2331 pairs show a local minimum at l=0.8.

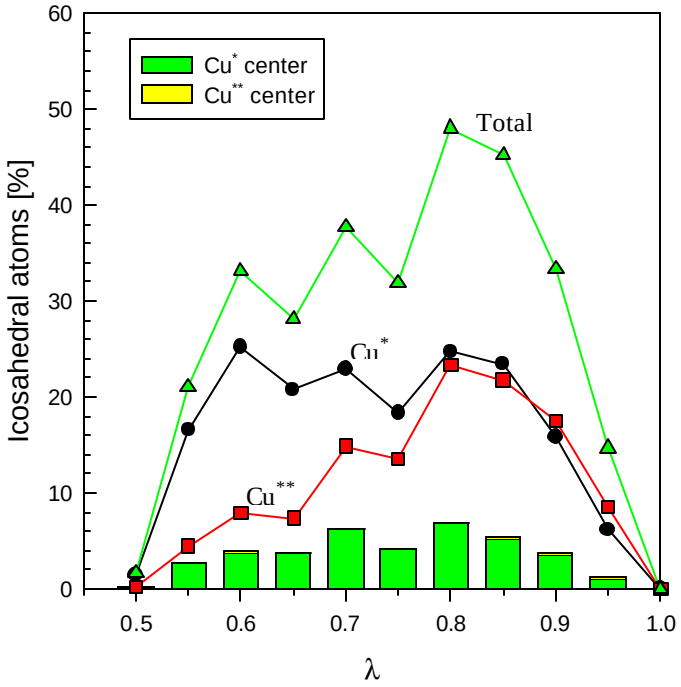

Figure 3-6(a). Binary system. The lines show the percentage of atoms contained in icosahedra either at the center (CN12 atoms) or at the surface as a function of l for T=300K at the end of the cooling run (cooling rate=$4x10^{12}$ K/s). The stacked bars show the number of CN12 center atoms. The total number of atoms in icosahedra is less than 13 times the number of center atoms because many icosahedra share atoms with other icosahedra. Interestingly, all of the CN12 center atoms are Cu^{*}, the smaller atom. For l>0.75, the concentration of Cu^{*} and Cu^{**} atoms in the icosahedra remains constant. For l=0.75, the concentrations are clearly disparate, with the icosahedra mostly associated with Cu^{*}.

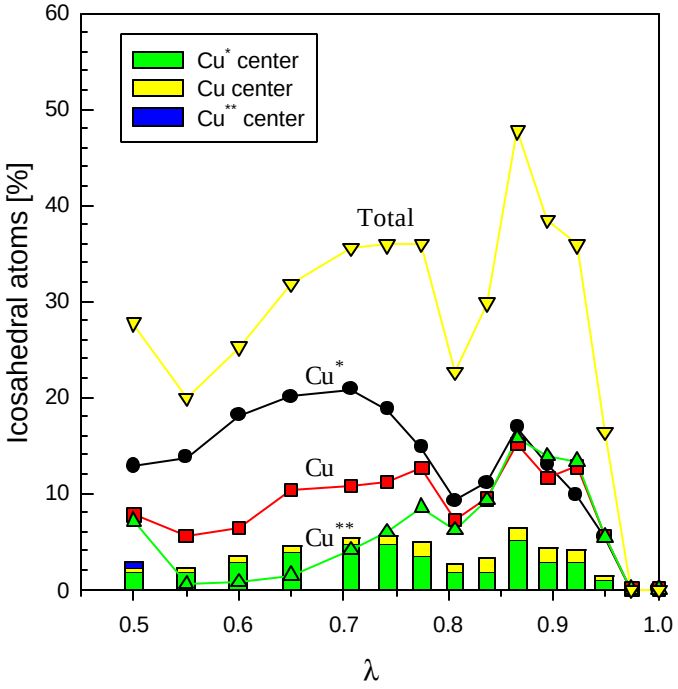

Figure 3-6(b). Ternary system. The number of CN12 center atoms are Cu^{*}>Cu>Cu^{**}. The concentrations of Cu^{*}, Cu, and Cu^{**} remain constant above l~0.8, while Cu^{**} rapidly disappears from icosahedra for smaller l.

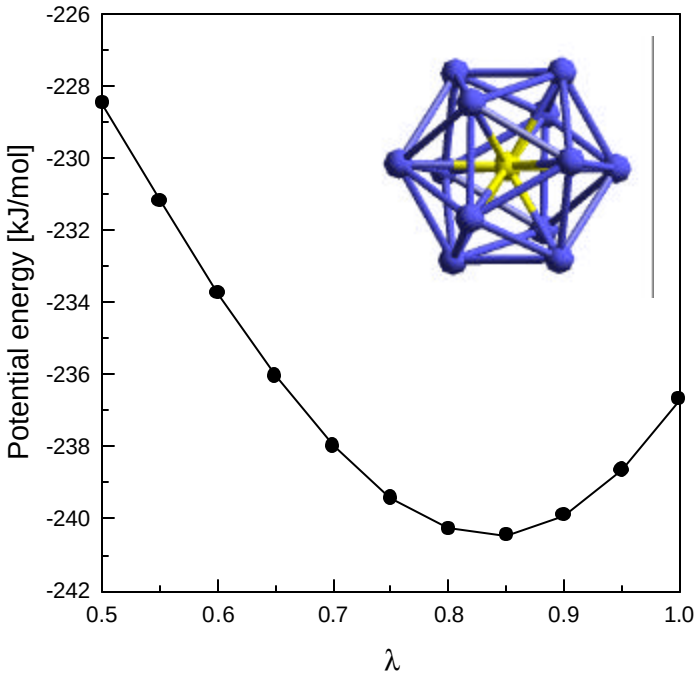

Figure 3-7. The minimum potential energy of 13-atom icosahedral cluster as a function of l. Here, Cu^{*} (light colored ball) is located in the center of the cluster and the 12 Cu^{**} atoms (dark colored ball) are located on the surface. The minimum energy is for l=0.838 as determined by a parabolic fit around the minimum.

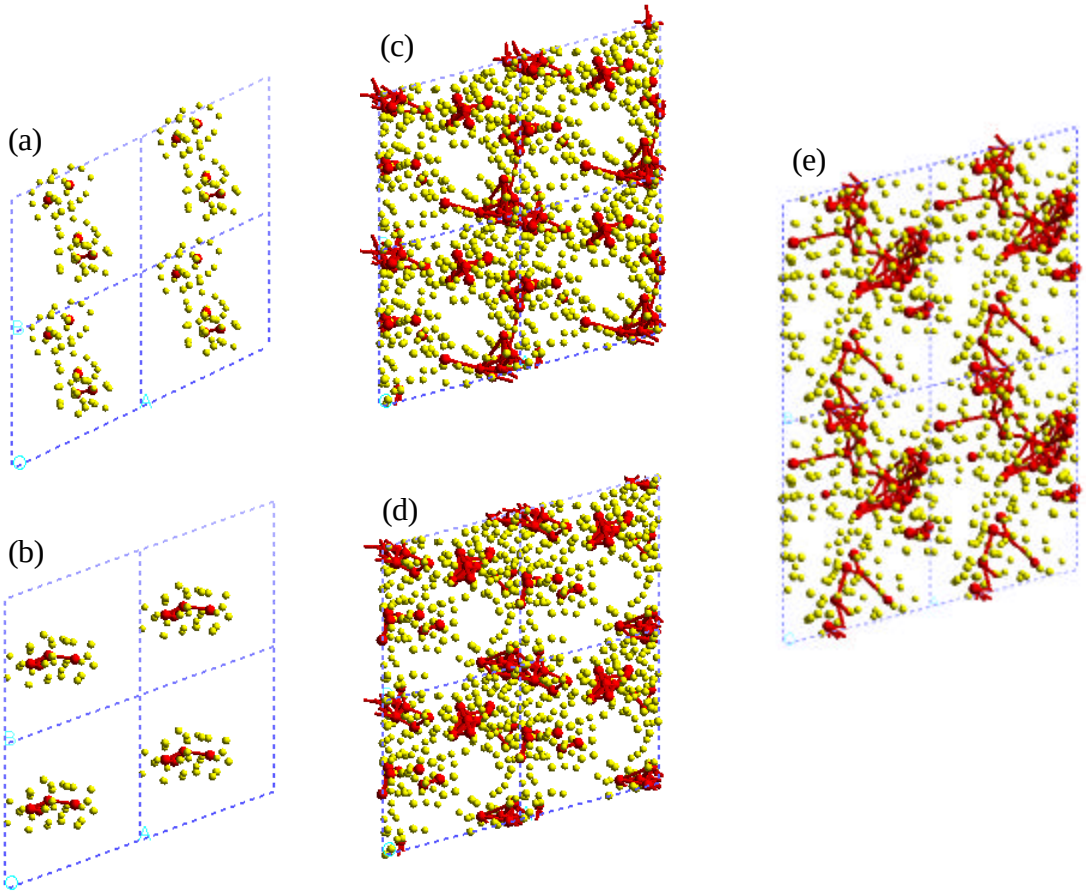

Figure 3-8. The topology of icosahedral ordering. Here, we show a projection of four unit cells on the xy plane. The centers of icosahedra are shown as dark balls and they are connected with a solid line if they interpenetrate (center atoms bonded, thus sharing five common neighbors, *i.e.*, 1551), share a face (center atoms share three common neighbor atoms, *i.e.*, 1331), share a line (center atoms share two common neighbor atoms), or share a vertex (center atoms share one common neighbor atom).

(a) $Cu^{*}_{50}Cu^{**}_{50}$ system with l=0.85, at T=800K, at time=0.1ps

(b) $Cu^{*}_{50}Cu^{**}_{50}$ system with l=0.85, at T=800K, at time=20.0ps

(c) $Cu^{*}_{50}Cu^{**}_{50}$ system with l=0.85, at T=300K, at time=0.1ps

(d) $Cu^{*}_{50}Cu^{**}_{50}$ system with l=0.85, at T=300K, at time=20.0ps

(e) $Cu^{*}_{33.3}Cu_{33.3}Cu^{**}_{33.3}$ system with l=0.86603, at T=300K, at time=20ps

(a)

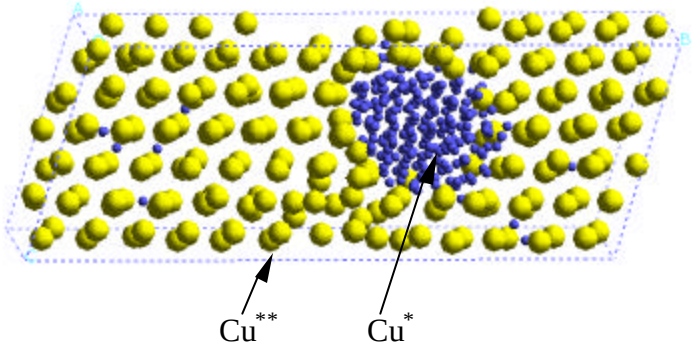

Figure 3-9. Binary alloy with l=0.50 at 300K after cooling from the liquid state (T=1600K). (a) A snapshot of one unit cell. Dark colored small balls are Cu^{*} and light colored big balls are Cu^{**}. Cu^{*} and Cu^{**} are phase separated with Cu^{**} showing crystalline order. (b) Partial radial distribution function (PRDF) of Cu^{*}, showing a predominance of amorphous packing (second peak split) but some FCC character. (c) PRDF of Cu^{**}showing FCC order.

(b)

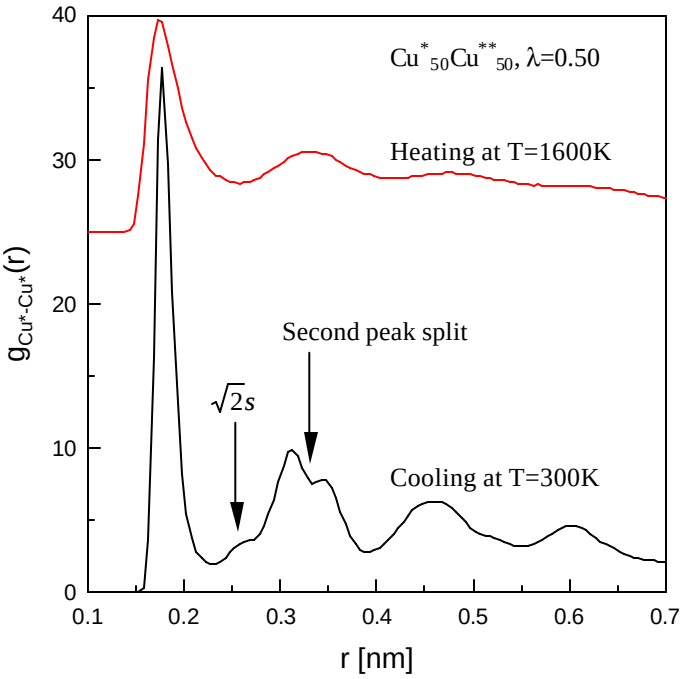
$Cu^{*}_{50}Cu^{**}_{50}$, λ=0.50
Heating at T=1600K
Second peak split
$\sqrt{2}s$
Cooling at T=300K
$g_{Cu^{*}\text{-}Cu^{*}}(r)$
r [nm]
0
10
20
30
40
0.1
0.2
0.3
0.4
0.5
0.6
0.7

(c)

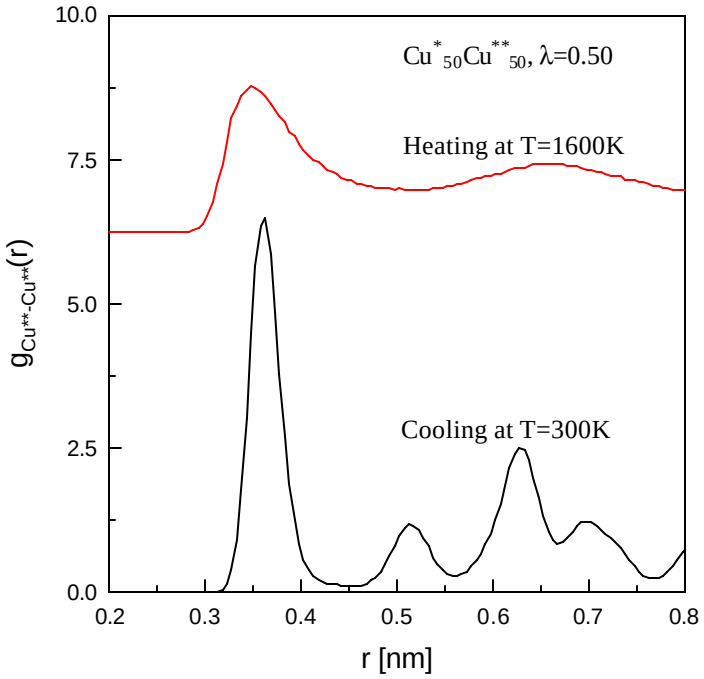
$Cu^{*}_{50}Cu^{**}_{50}$, λ=0.50
Heating at T=1600K
Cooling at T=300K
$g_{Cu^{**}\text{-}Cu^{**}}(r)$
r [nm]
0.0
2.5
5.0
7.5
10.0
0.2
0.3
0.4
0.5
0.6
0.7
0.8

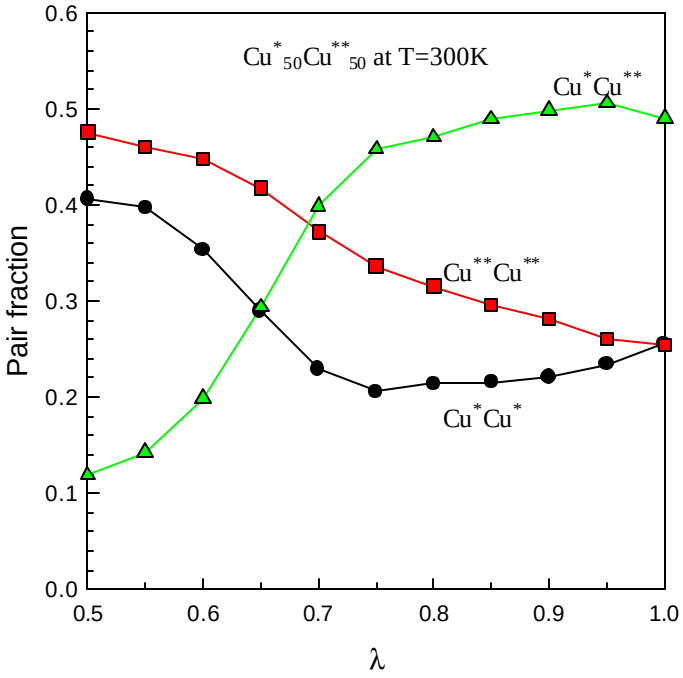

Figure 3-10. The pair fraction in the binary system as a function of l. The fraction of unlike pairs (Cu^{*}-Cu^{**}) is nearly constant above l~0.75, but decreases rapidly below 0.75, indicating the onset of phase separation.

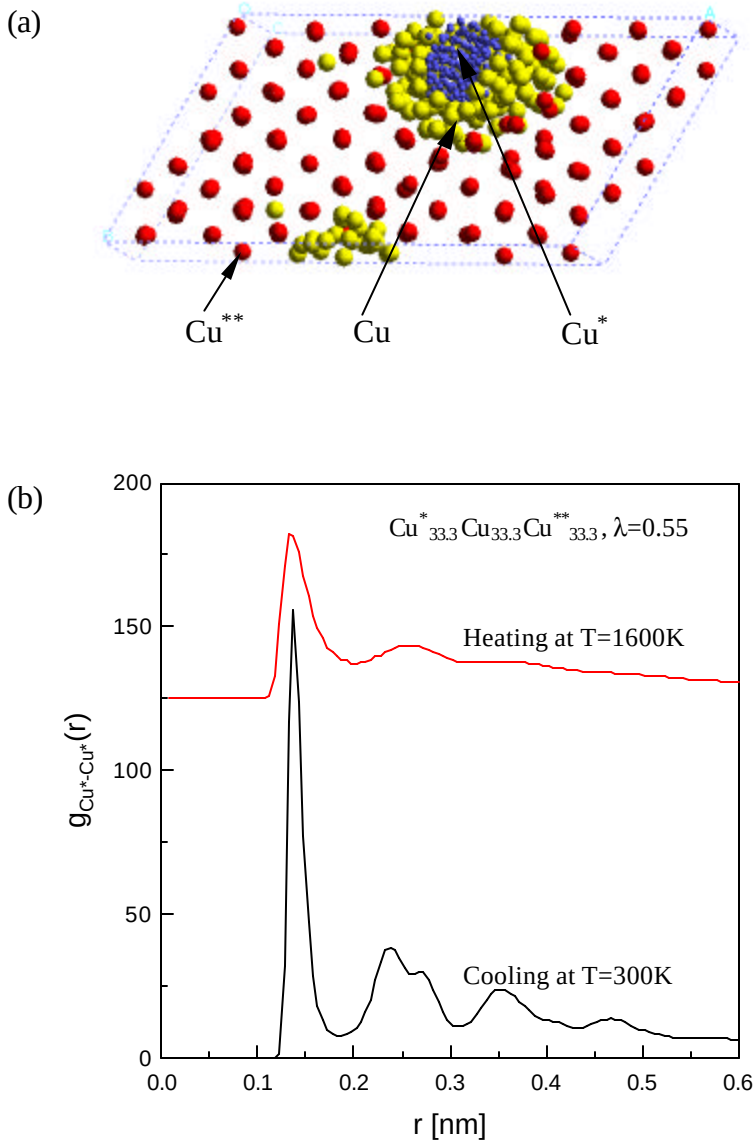

Figure 3-11. The ternary alloy with l=0.55 at 300K after cooling from the liquid state (T=1600K). (a) A snapshot of one unit cell. Dark colored small balls are Cu^{*}, light colored big balls are Cu and dark colored big balls are Cu^{**}. Cu^{*}, Cu and Cu^{**} are phase separated with Cu^{**} showing crystalline order. (b) PRDF of Cu^{*} shows amorphous packing at T = 300K. (c) PRDF of Cu shows amorphous packing at T = 300K. (d) PRDF of Cu^{**} shows FCC order at T = 300K.

(c)

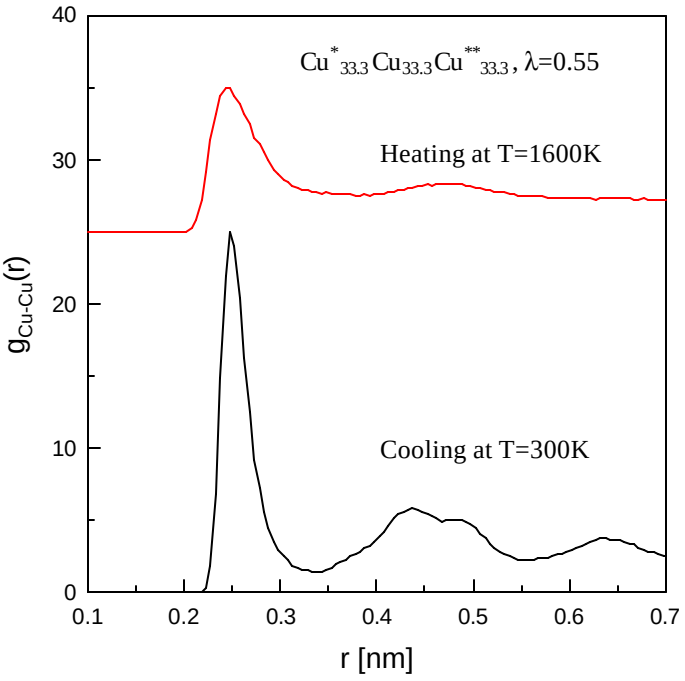
$Cu^{*}_{33.3}Cu_{33.3}Cu^{**}_{33.3}$, λ=0.55
Heating at T=1600K
Cooling at T=300K
$g_{Cu-Cu}(r)$
r [nm]
0
10
20
30
40
0.1
0.2
0.3
0.4
0.5
0.6
0.7

(d)

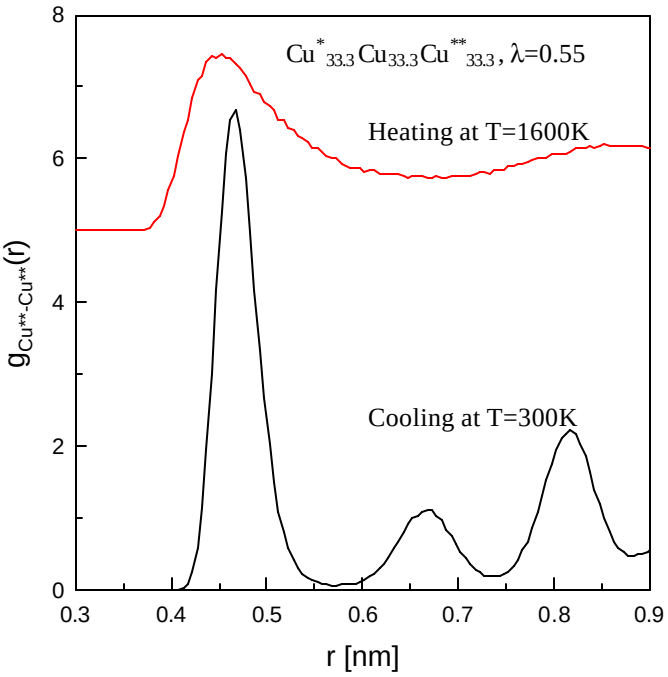
$Cu^{*}_{33.3}Cu_{33.3}Cu^{**}_{33.3}$, λ=0.55
Heating at T=1600K
Cooling at T=300K
$g_{Cu^{**}-Cu^{**}}(r)$
r [nm]
0
2
4
6
8
0.3
0.4
0.5
0.6
0.7
0.8
0.9

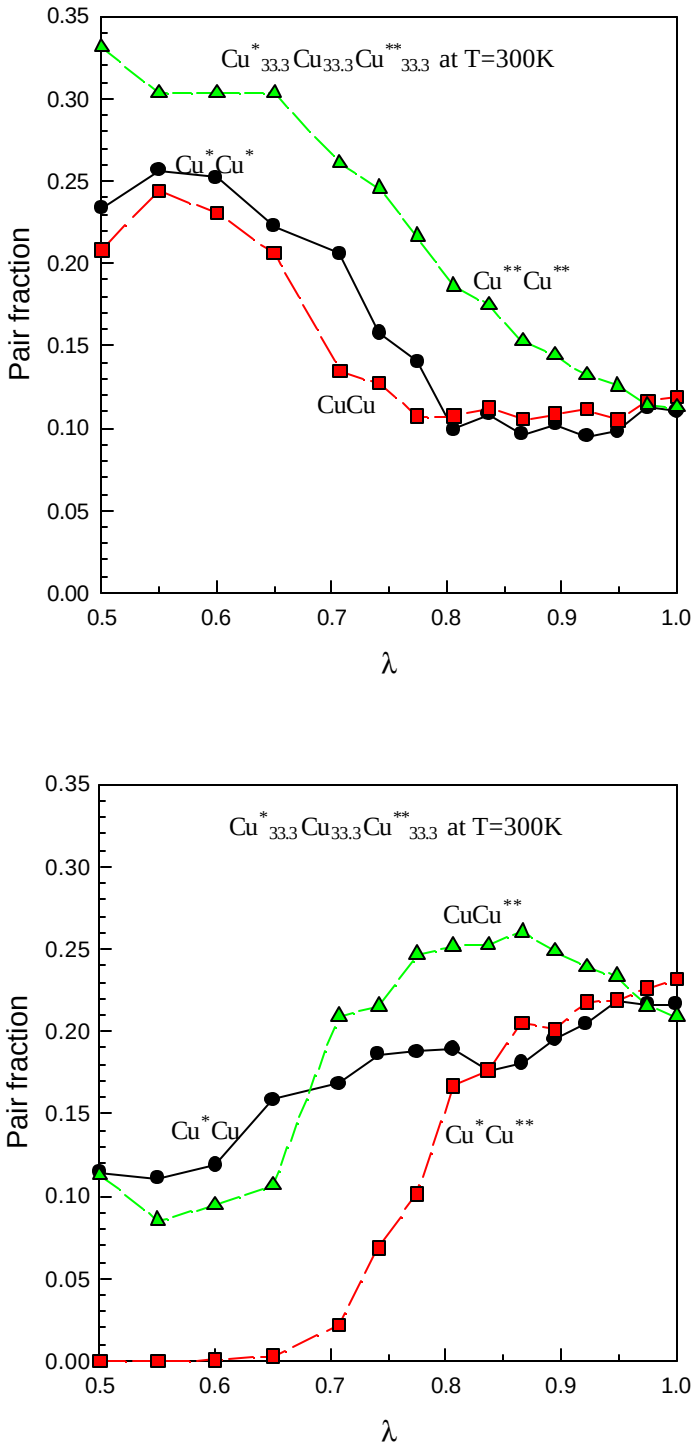

Figure 3-12. The pair fraction in the ternary system as a function of l. (a) Like pairs (Cu^{*}-Cu^{*}, Cu-Cu, and Cu^{**}-Cu^{**}). (b) Unlike pairs (Cu^{*}-Cu, Cu^{*}-Cu^{**}, and Cu-Cu^{**}).